Acta Astronautica 194 (2022) 323–333

Contents lists available at ScienceDirect

Acta Astronautica

journal homepage: www.elsevier.com/locate/actaastro

Research paper

Balancing differential drag with Coulomb repulsion in low earth orbit plasma wakes

Jordan Maxwell [*,1], Andrew Harris [1], Hanspeter Schaub [2]

Colorado Center for Astrodynamics Research, 3775 Discover Drive, 429 UCB University of Colorado, Boulder, CO 80303, United States of America

ABSTRACT

A novel method for close-proximity formation flying under differential atmospheric drag using Coulomb forces is investigated for applications in Earth sensing, space-situational awareness (SSA), and aeronomy. Objects in LEO are supersonic with respect to the ambient environment, creating a thinned out wake region behind the craft as it travels through the ionosphere. Objects within this wake experience little drag acceleration and are able to attain voltages much greater than in the ambient ionospheric plasma, creating implications for the design and control of close-proximity leader–follower spacecraft pairs. The proposed system consists of a leader craft with a set of affixed, conducting spheres and a charged follower craft located in the wake of the leader. The differential drag acceleration between the leader and follower craft is countered by a controlled Coulomb repulsion to maintain precise separation. The charged structure on the rear of the leader craft is designed such that the charged follower craft sits in an electrostatic potential well which opposes off-axis perturbations. A conceptual method for controlling such a pair without the use of propellant using a set of charged spheres is investigated, with nonlinear models of the system's relative motion derived and discussed. Linearized models are used to demonstrate the local controllability of the system to demonstrate the proposed system's merit. This linear analysis is used to derive conditions on controllability and control performance under different charge geometries and environmental assumptions.

1. Introduction

Close-proximity formation flying is an enabling technology for next-generation missions involving space situational awareness, spacecraft servicing [1], debris mitigation, or Earth observation. However, close-proximity formation flight represents a substantial challenge to spacecraft guidance, navigation, and control technologies, especially when tight position constraints are imposed by one of the aforementioned mission types. The use of traditional thrusters for formation-flight control increases mission mass and cost; additionally, thruster plumes for close-proximity flight can cause undesirable effects due to plume impingement on neighboring spacecraft. By fusing concepts from differential-drag formation flight and Coulomb-actuated formation flight, this work aims to demonstrate the feasibility of non-impulsive formation flight that leverages the space environment to achieve tight formation control tolerances.

Traditional approaches to close-proximity formation flight consider the application of impulsive thrusters as actuators. The CanX-4/5 dual spacecraft experiment utilized a pair of nanosatellites to achieve sub-meter level control accuracy while using between 1.15 and 3.40 cm/s of ΔV per orbit [2]. While these values are small, they imply that a multi-year formation flight mission would require hundreds of meters per second of ΔV, which would require steep trade-offs from other mission areas. For these reasons, it is desirable for future high-precision formation flight missions to leverage forces originating from the space environment whenever possible.

The study of environmental forces for formation actuation is substantial. For spacecraft in LEO, drag forces are a dominant perturbation force [3]. Differential drag formation flight, which uses differences in drag forces acting on spacecraft to achieve relative accelerations, has been used to constitute and maintain formations operationally as described by Foster [4]. However, uncertainty in forecasts of atmospheric density [5] and spacecraft drag coefficients [6], combined with the small magnitude of drag forces, has thus far precluded their application to the high-precision formation flight domain.

While drag is usually considered in terms of number density in LEO, it is important to recognize that two populations of massive particle exist in this region — ions and neutrals. Recent work in the field of charged astrodynamics demonstrates that the drag acceleration on LEO spacecraft resulting from collisions with plasma ions can be modulated via electromagnetic fields to augment the total drag acceleration. In fact, it has been shown that for given altitudes and spacecraft voltages, the ion component of the drag acceleration can dominate over that of neutrals. [7] This finding demonstrates one application of electrostatics on orbit.

Charging of two resident space objects via passive and active means results in Coulomb forces that represent another method of

---

[*] Corresponding author.

E-mail addresses: Jordan.Maxwell@Colorado.edu (J. Maxwell), Andrew.Harris@Colorado.edu (A. Harris), Hanspeter.Schaub@Colorado.edu (H. Schaub).

[1] Graduate Research Assistant.

[2] Glenn L. Murphy Endowed Chair.

https://doi.org/10.1016/j.actaastro.2020.08.021
Received 28 February 2019; Received in revised form 17 July 2020; Accepted 18 August 2020

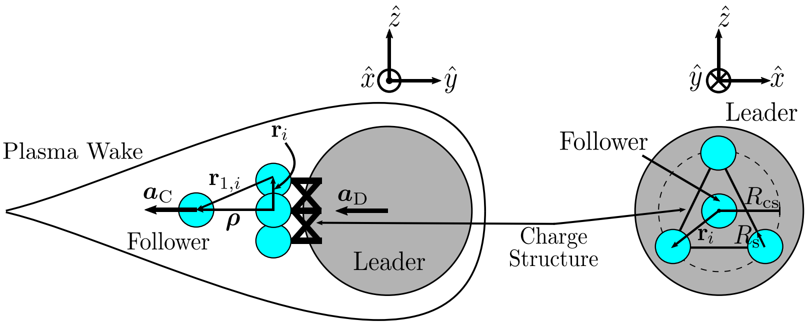

Fig. 1. Off-axis (left) and on-axis (right) views of the Coulomb-balanced differential drag concept. Axes indicate the Hill–Clohessy–Wiltshire (HCW) frame directions as defined in Section 2.2.

zero-propellant maneuvering for formation flight. First described by Ref. [8], Coulomb formation flight is largely considered in the context of GEO formation flight [9] due to the need for low plasma densities to prevent charge dispersion and plasma shielding effects. Multiple studies have demonstrated the controllability of formations where individual spacecraft are considered as charged spheres [10]. The Multi Sphere Method [11] (MSM) allows for fast and rapid estimation of the electric field about craft by modeling them as a collection of charged spherical elements. The technique has recently been expanded for application to time-varying structures [12]. The presence of relatively dense ambient plasmas in LEO prevents extreme spacecraft charging by providing a medium for charge transfer and as a result few studies in the use of Coulomb actuation for LEO formation flight have been undertaken. Additionally, the Debye length in LEO plasma – the spatial scale over which an electric potential decays by $\frac{1}{e}$ in a plasma – is on the order of 1 cm, so electrostatic forces and torques are attenuated significantly beyond this distance.

Investigations of the dynamics of spacecraft plasma wakes – regions of decreased plasma density produced behind spacecraft as they move through space – suggests that GEO-like plasma environments exist behind spacecraft in LEO. For a spherical craft at the plasma floating potential in LEO, the plasma wake roughly takes the shape of a right cone extending one body radius behind the spacecraft [13]. This density reduction applies to both plasma and neutral species, reducing drag forces acting on spacecraft in the wake, creating relative accelerations due to differential drag. Recent experimental work has demonstrated that, by charging spacecraft components positively, the plasma component of the wake can be expanded relative to the neutral wake generated by that component, providing a larger working volume for electrostatic actuation techniques [14]. Ref. [15] provides a framework for scaling these interactions, expanding the insight derived from these experiments.

A primary motivator for the use of electrostatic actuation in LEO was the investigation of an astronaut in the wake of the Space Shuttle detailed in Ref. [16]. Hall et al. used the NASCAP charging code to simulate the charging of a modeled astronaut in the wake while passing through the aurorae, and found that charge levels as high as −6 kV were possible — this voltage could generate significant forces and torques on a nearby charged object. While a detailed analysis of the wake dynamics resulting from this large potential was not undertaken, this result implies that significant charge levels can be achieved in the wake, providing a foundation for the investigation of electrostatic actuation techniques in LEO.

This investigation described herein envisions a formation flight system that leverages the unique physics of the wake by applying Coulomb repulsion to balance differential drag effects and thereby enable high-precision, close-proximity formation flight in LEO. The assumption that the high density, low temperature plasma environment in LEO would utterly preclude electrostatic actuation techniques has, until now, led researchers to discount the applicability of the method to this orbit. This paper presents novel results in the field of electrostatic actuation which demonstrate that highly-precise formation keeping can be accomplished in LEO-like conditions with this technique using reasonably small craft potentials, even under significant perturbations and sensor noise.

This work is arranged as follows. First, the architecture of the proposed formation flight system is presented alongside bounding assumptions. Next, the non-linear dynamics of such a system are derived from first principles. These dynamics are then linearized about an equilibrium condition that uses Coulomb repulsion to counter-act drag forces acting on the leader spacecraft. The linear controllability of this system is examined for a variety of feasible system parameters and assumed drag accelerations. Finally, a representative, controlled system is demonstrated using the true non-linear dynamics under additional non-modeled perturbations to validate this approach.

2. Problem statement

2.1. System configuration

A two-spacecraft, leader–follower formation in Low Earth Orbit (LEO) is considered in this work, which aims to study the feasibility of Coulomb-balanced differential-drag formation flight in LEO spacecraft wakes. The Displaced Phase Center Antenna (DPCA) [17,18] concept is used as a frame for this investigation, providing notional mission scenario parameters as well as one of several motivations for the development of the proposed technique. Prior studies in DPCA mission design have shown a required baseline offset on the order of meters – providing a configuration appropriate to the volumetric constraints of a LEO plasma wake – with this relative rectilinear position being held to sub-centimeter accuracy. These parameters are considered as bounding constraints to inform the parameters considered by this study.

The mission concept is illustrated in Fig. 1. A charge structure consisting of n_cs conducting spheres at positions $\boldsymbol{r}_i$ spaced equally about a circle of radius R_cs is attached to the rear of the leader craft. For this investigation, all conducting spheres have the same radius R_s, which is constrained to be smaller than $\sin\left({}^{180^\circ}\!/_{n_\mathrm{cs}}\right) R_\mathrm{cs}$ such that no two adjacent spheres touch, as this would cause them to remain at equipotential. In practice, R_s is chosen smaller than this limit, as larger separations between conducting spheres mitigates the possibility of arcing events and reduces the magnitude of higher-order charging effects not accounted for in the MSM model applied. The charge structure configuration creates an electrostatic potential well behind the leader craft, pictured in terms of an electric field in Fig. 2 and calculated using Eq. (11).

A charged follower craft is offset in the along-track direction by some distance ρ_f. A requirement of the electrostatic actuation technique is that the follower craft must be small compared to the wake of the leader. While this system configuration does not strictly adhere to the current literature on DPCA, it is assumed the technique is feasible with the formation in Fig. 1. In general, the follower craft can be modeled with many spheres, but for this initial investigation a single-sphere model is chosen. It is important to note that the follower craft

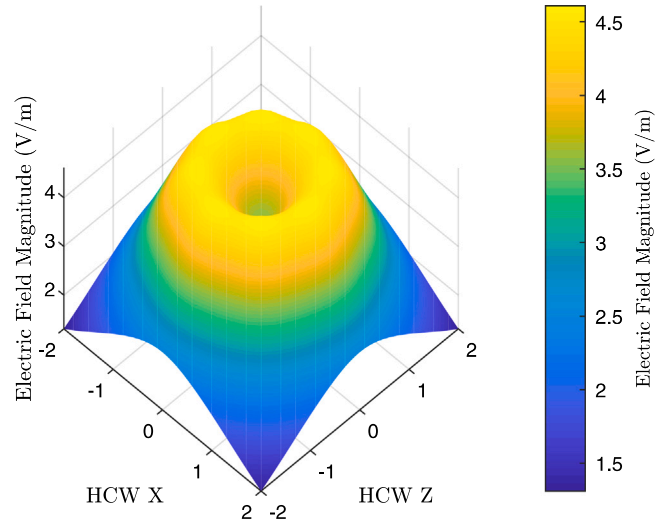

Fig. 2. The electric field 1 m behind the charge structure for a configuration in which $n_{cs} = 8$, $R_{cs} = 1$ m. Reference Fig. 1 for axis directions.

is assumed to have been put in this position by some alternative actuation technique, as electrostatic actuation only functions on close proximity craft. Nominally, the follower sits directly in the center of the electrostatic potential well in Fig. 2, so that only in the anti-alongtrack direction is a repulsive force felt. Should any unmodeled perturbation provide off-axis accelerations, the structure of the potential well naturally provides a restoring acceleration, though control is also applied in such a case. This does not indicate that the system is stable without control, as only off-axis perturbations generate a restoring acceleration.

Because the wake exhibits decreased neutral density as well as plasma density, the drag acceleration on the follower is assumed to be zero. Differential drag will always decrease the separation between the leader and follower in this case, so voltages are sourced on the follower and charge structure to cancel the drag acceleration of the leader. Negative voltages are chosen because the wake is only ion devoid — the presence of electrons means that negative voltages will require less power than positive ones. Additionally, shielding of negatively signed potentials in an electron-dominated plasma is significantly less than that of those positive [19]. Therefore, the wake acts as vacuum for negative potentials. A pusher-only control is used in which the controller only ever sources repulsive Coulomb forces. If the follower exceeds the nominal separation, the voltages are nulled and differential drag brings the craft back together. For this investigation, it is assumed beforehand that the extremely tight DCPA-imposed tolerance on relative position will also require the craft to remain in the wake — it is demonstrated in later sections that this is indeed the case. This investigation focuses on feasibility of the mission concept and control scheme and, as such, the wake is taken to behave as vacuum. This assumption is validated in part by Ref. [19], but the effects on wake geometry and properties resulting from placing charged objects within are outside the scope of this preliminary study and are therefore neglected.

MSM is applied to calculate the Coulomb acceleration between the leader and follower crafts. This modeling method is especially well-suited to the proposed technique, given the arrangement of charged spheres. However, for simplicity and computational efficiency, nearby charge spheres are considered as point sources for all mutual effects. The higher-order effects resulting from complicated charge distributions are again considered out-of-scope for this study.

2.2. Frame definitions & notation

The two frames used throughout the problem described above are the Earth Centered Inertial (ECI) frame and the Hill–Clohessy–Whiltshire (HCW) frame, denoted $\mathcal{N}$ and $\mathcal{H}$, respectively. The formal definitions of the frames are provided below where $\hat{\boldsymbol{n}}_i$ signifies an inertial unit vector, $\hat{\boldsymbol{r}}_{\mathrm{L}}$ is the leader's normalized position relative to the center of the Earth, and $\hat{\boldsymbol{h}}_{\mathrm{L}}$ is the direction of the leader's angular momentum vector.

$$\mathcal{N} : \{\mathcal{O}_{\mathrm{E}}, \hat{\boldsymbol{n}}_1, \hat{\boldsymbol{n}}_2, \hat{\boldsymbol{n}}_3\} \ , \ \mathcal{H} : \{\mathcal{O}_{\mathrm{L}}, \hat{\boldsymbol{r}}_{\mathrm{L}}, \hat{\boldsymbol{h}}_{\mathrm{L}} \times \hat{\boldsymbol{r}}_{\mathrm{L}}, \hat{\boldsymbol{h}}_{\mathrm{L}}\} \tag{1}$$

The origin of the ECI frame ($\mathcal{O}_{\mathrm{E}}$) is Earth's center, while the HCW frame center ($\mathcal{O}_{\mathrm{L}}$) is at leader craft's center of mass.

Throughout this paper, bolded quantities indicate vectors. A left superscript indicates the frame in which a given vector is defined, while the hat notation indicates a unit vector (i.e. ${}^{\mathcal{N}}\hat{\boldsymbol{x}}$ indicates the unit vector of $\boldsymbol{x}$ expressed in the inertial frame). In general, matrices are signified via square brackets, though Direction Cosine Matrices (DCMs) are identified, for example, by the form $[\mathcal{HN}]$ indicating the mapping of a right multiplied vector from the inertial to the Hill frame.

$${}^{\mathcal{H}}\boldsymbol{x} = [\mathcal{HN}]{}^{\mathcal{N}}\boldsymbol{x} \ , \ [\mathcal{HN}] = [{}^{\mathcal{H}}\hat{\boldsymbol{n}}_1, {}^{\mathcal{H}}\hat{\boldsymbol{n}}_2, {}^{\mathcal{H}}\hat{\boldsymbol{n}}_3] \tag{2}$$

Finally, a notation for time derivatives as seen by different frames is introduced.

$$\dot{\boldsymbol{x}} = {}^{\mathcal{N}}\frac{\partial \boldsymbol{x}}{\partial t} \ , \ \boldsymbol{x}' = {}^{\mathcal{H}}\frac{\partial \boldsymbol{x}}{\partial t} \tag{3}$$

Additional notations will be introduced throughout the text, but the definitions above provide a baseline for beginning the analysis.

3. Nonlinear equations of motion

Four perturbations are included in the simplified model used to simulate the environment: Coulomb forces, two-body gravity, orbital drag, and Solar Radiation Pressure (SRP). For the following discussion, it is useful to define $\boldsymbol{\rho}$ as the difference of the positions of the leader and follower.

$$\boldsymbol{\rho} = \boldsymbol{r}_{\mathrm{f}} - \boldsymbol{r}_{\mathrm{L}} \tag{4}$$

3.1. Coulomb acceleration

The Coulomb acceleration of the follower relative to the leader is calculated from the charge and mass of the follower — Q_{f} and m_{f}, respectively — and the electric field of the leader $\boldsymbol{E}_{\mathrm{L}}$ generated by the charge structure pictured in Fig. 1.

$$\boldsymbol{a}_{\mathrm{C}}(\boldsymbol{X}, \boldsymbol{V}) = \frac{1}{m_{\mathrm{f}}} Q_{\mathrm{f}} \boldsymbol{E}_{\mathrm{L}}(\boldsymbol{X}, \boldsymbol{V}) \tag{5}$$

The proximity of the follower to the charge structure on the leader means that a mutual capacitance exists between the two objects. This effect is described by the relation between the voltage and the charge on a given object. The voltage V_i on a given sphere subject to its own charge Q_i and the charge Q_j on nearby spheres is calculated.

$$V_i = k_{\mathrm{C}} \frac{Q_i}{R_i} + k_{\mathrm{C}} \sum_{j=1, j \neq i}^{n} \frac{Q_j}{r_{i,j}} \tag{6}$$

Here, $k_{\mathrm{C}} = 8.99 \times 10^9$ Nm^2/C^2 is Coulomb's constant, R_i is the radius of the ith sphere, and $r_{i,j}$ is the center-to-center distance between the ith and jth spheres. Throughout this paper, the subscript 1 refers to the follower and subscripts 2 through n refer to the spheres on the charge structure. The relation above can be rewritten into a single matrix equation.

$$\begin{pmatrix} V_1 \\ V_2 \\ \vdots \\ V_n \end{pmatrix} = k_{\mathrm{C}} \begin{bmatrix} {}^1/R_1 & {}^1/r_{1,2} & \dots & {}^1/r_{1,n} \\ {}^1/r_{2,1} & {}^1/R_2 & \dots & {}^2/r_{2,n} \\ \vdots & \vdots & \ddots & \vdots \\ {}^1/r_{n,1} & {}^1/r_{n,2} & \dots & {}^1/R_n \end{bmatrix} \begin{pmatrix} Q_1 \\ Q_2 \\ \vdots \\ Q_n \end{pmatrix} \tag{7}$$

Written in a more compact fashion

$$\boldsymbol{V} = [S]\boldsymbol{Q} \tag{8}$$

where $[S]$ is the elastance matrix [20]. Another well-known expression relating charge to voltage, $\mathbf{Q} = [C]\mathbf{V}$ indicates that the capacitance is the inverse of the elastance matrix.

$$\mathbf{Q} = [S]^{-1}\mathbf{V} \tag{9}$$

This form is preferable, as the voltage is the control variable and the charge dictates the dynamics. The charge on the follower can be written as an inner product between the first row of the capacitance and the voltage vector. As displayed in Fig. 1, the follower craft is simulated as a single sphere, though in general Q_{f} in Eq. (5) represents the total charge on a follower simulated with n MSM spheres.

$$Q_{\mathrm{f}} = Q_1 = \boldsymbol{C}_1^T\boldsymbol{V} \tag{10}$$

The vector $\boldsymbol{C}_i$ indicates the ith row of the capacitance matrix. The electric field from the charge structure $\boldsymbol{E}_{\mathrm{L}}$ at the position of the follower can be calculated by summing the individual fields from each of the spheres on the charge structure.

$$\boldsymbol{E}_{\mathrm{L}}(\boldsymbol{X},\boldsymbol{V}) = k_{\mathrm{C}}\sum_{i=2}^{n}\frac{\boldsymbol{C}_i^T\boldsymbol{V}}{r_{1,i}^3}\boldsymbol{r}_{1,i} \tag{11}$$

Note that the vector pointing from the ith sphere to the follower can be written in terms of the state variable ($\boldsymbol{r}_{1,i} = \boldsymbol{\rho} - \boldsymbol{r}_i$). Substituting Eqs. (10) and (11) into (5) yields the non-linear acceleration of the follower subject to the leader.

$$\boldsymbol{a}_{\mathrm{C}}(\boldsymbol{X},\boldsymbol{V}) = \frac{k_{\mathrm{C}}}{m_{\mathrm{r}}}\boldsymbol{C}_1^T\boldsymbol{V}\sum_{i=2}^{n}\frac{\boldsymbol{C}_i^T\boldsymbol{V}}{r_{1,i}^3}\boldsymbol{r}_{1,i} \tag{12}$$

An additional complication presents itself in Eq. (12). The coupling through the mutual capacitance described by Eq. (7) means that the proximity of two nearby objects affects their charge. To demonstrate this affect, Eq. (10) is expanded. The dual subscripts $C_{i,j}$ indicate the position of a scalar element within the capacitance matrix.

$$Q_1 = \boldsymbol{C}_1^T\boldsymbol{V} = C_{1,1}V_1 + \sum_{i=2}^{n}C_{1,i}V_i \tag{13}$$

By convention, the self capacitance of an object ($C_{1,1}$) is always positive, while the mutual capacitance terms ($C_{1,i}$) are always negative, though both are position-dependent quantities [20]. Physically, this results in nearby objects of the same voltage causing a decrease in charge on – in this case – the follower craft. This means that there are sets of voltages and relative positions for which a large enough Coulomb acceleration cannot be generated to counter differential drag.

To demonstrate this, consider the mission scenario discussed above and recall that the Coulomb accelerations between the leader and follower are proportional to the charge products. The norm of Eq. (12) is expanded below. For the purpose of clearly explaining the limits on attainable voltages, all charge structure spheres are assumed to have the same potential V_2. As discussed previously, the desired Coulomb acceleration is that which perfectly opposes the drag acceleration in the along-track direction (a_{Drag_y}).

$$\|\boldsymbol{a}_{\mathrm{C}}(\boldsymbol{X},\boldsymbol{V})\| = -a_{\mathrm{Drag}_y} = Q_{\mathrm{f}}E_{\mathrm{L}} \tag{14}$$

The follower charge Q_{f} is calculated as in Eqs. (10) and (13). To calculate the magnitude of the leader electric field magnitude E_{L}, consider the nominal system geometry applied in this analysis shown in Fig. 1 shown for a three-sphere charge structure. For this nominal configuration, the distances $r_1 = \sqrt{R_{cs}^2 + \rho^2}$ between the follower and each of the charge structure spheres are identical. While it is difficult to show mathematically for a n_{cs}-sphere charge structure, the symmetry of the system makes it clear that the charge structure charges Q_2 are equal given the assumptions that they are at equipotential. The physical rationale for this is that the capacitance matrix is purely geometrical, and the system geometry looks identical from the perspective of each of the charge structure spheres. Substituting these conditions into Eq. (11) the electric field of the leader can be simplified.

$$\boldsymbol{E}_{\mathrm{L}} = \frac{k_{\mathrm{C}}Q_2}{r_1^3}\sum_{i=2}^{n}\boldsymbol{r}_{1,i} \tag{15}$$

Note from the system geometry in Fig. 1 that the system exhibits n_{cs}-fold symmetry about the $\hat{\boldsymbol{h}}_2$ axis. This results in the sum of vectors $\boldsymbol{r}_{1,i}$ having components only along this axis. The electric field is finally written without summations given the projection of $\boldsymbol{r}_{1,i}$ onto $\hat{\boldsymbol{h}}_2$ is ρ.

$$\boldsymbol{E}_{\mathrm{L}} = \frac{k_{\mathrm{C}}Q_2}{r_1^3}\sum_{i=2}^{n}\boldsymbol{r}_{1,i} = n_{cs}k_{\mathrm{C}}Q_2\frac{\rho}{r_1^3}\hat{\boldsymbol{h}}_2 \tag{16}$$

The equation above matches physical intuition: the superpositional nature and geometric symmetry means that the electric field components in the HCW-X and -Z directions cancel. The charge structure charge can be calculated in a variety of ways but is taken as $Q_2 = C_{2,1}V_1 + V_2\sum_{j=2}^{n}C_{2,j}$. Finally, Eq. (14) is expanded given the follower charge Q_{f} and leader electric field E_{L} expressions.

$$-a_{\mathrm{Drag}_y} = \frac{n_{cs}\rho k_{\mathrm{C}}}{r_1^3 m_{\mathrm{f}}}\left(C_{1,1}V_1 + V_2\sum_{i=2}^{n}C_{1,i}\right)\left(C_{2,1}V_1 + V_2\sum_{j=2}^{n}C_{2,j}\right) \tag{17}$$

This equation can be re-expressed as a quadratic in V_2, assuming a charge structure voltage is desired to be found for a given follower voltage V_1. The following substitutions are made to simplify the equation. Recall the discussion of the signs of self and mutual capacitance previous.

$$\begin{aligned} \alpha &= C_{1,1} > 0 \\ \beta &= \sum_{i=2}^{n}C_{1,i} < 0 \\ \gamma &= C_{2,1} < 0 \\ \delta &= \sum_{j=2}^{n}C_{2,j} < 0 \end{aligned} \tag{18}$$

Eq. (17) is written as a quadratic in V_2.

$$0 = \beta\delta V_2^2 + (\alpha\delta + \beta\gamma)V_1V_2 + (\alpha\gamma V_1^2 + \frac{r_1^3 m_{\mathrm{f}}}{n_{cs}\rho k_{\mathrm{C}}}a_{\mathrm{Drag}_y}) \tag{19}$$

The condition on real voltages satisfying this expression come from the square root term in the quadratic equation. This condition is written

$$(\alpha\delta + \beta\gamma)^2V_1^2 - 4\beta\delta(\alpha\gamma V_1^2 + \frac{r_1^3 m_{\mathrm{f}}}{n_{cs}\rho k_{\mathrm{C}}}a_{\mathrm{Drag}_y}) > 0 \tag{20}$$

Solving for V_1 yields the final condition for the minimum follower voltage.

$$V_1^2 > \frac{4\beta\delta r_1^3 m_{\mathrm{f}}a_{\mathrm{Drag}_y}}{n_{cs}\rho k_{\mathrm{C}}(\alpha\delta - \beta\gamma)^2} \tag{21}$$

Note here that, given the sign of the substituted variables indicated in Eq. (18), there is a minimum follower voltage for all possible configurations. Two possible solutions exist for the minimum follower voltage with equal magnitude and opposite sign, which corresponds to the fact that both mutually positive and mutually negative objects produce repulsive forces. Note that the solution for V_2 also requires a quadratic, resulting in a similar sign ambiguity. Given knowledge of the sign of a_{Drag_y}, it is known that V_1 and V_2 must have the same sign.

3.2. Orbital perturbations

While the control formulation incorporates linearized two-body gravity, drag, and Coulomb accelerations, the true simulated environment consists of nonlinear two-body gravity, drag, and Solar Radiation Pressure (SRP) accelerations. For each spacecraft, the gravitational acceleration is calculated given the gravitational constant of Earth μ and the position relative to the center of Earth $\boldsymbol{r}$.

$$\boldsymbol{a}_{\mathrm{G}} = -\frac{\mu}{r^3}\boldsymbol{r} \tag{22}$$

Canonball drag and SRP models are used, as spherical craft are assumed in the scenario. The drag model used is shown below where A is the cross-sectional area, m the mass, C_{D} the drag coefficient, ρ_{atm} the local atmospheric density, and $\boldsymbol{v}_{\mathrm{rel}} = \dot{\boldsymbol{r}} - \boldsymbol{\omega} \times \boldsymbol{r}$ the atmosphere-relative velocity of a given craft with orbit angular velocity $\boldsymbol{\omega}$. For this simulation, a corotating atmosphere is assumed rotating at earth's angular velocity (ω_{E}) such that $\boldsymbol{\omega} = \omega_{\mathrm{E}}\hat{\boldsymbol{h}}_{\mathrm{L}}$.

$$\boldsymbol{a}_{\mathrm{D}} = -\frac{1}{2}\frac{AC_{\mathrm{D}}\rho_{\mathrm{atm}}}{m}v_{\mathrm{rel}}^2\hat{\boldsymbol{v}}_{\mathrm{rel}} \tag{23}$$

Here, $\boldsymbol{v}_{\mathrm{rel}} = \dot{\boldsymbol{r}} - \boldsymbol{\omega} \times \boldsymbol{r}$. The model used for SRP is calculated

$$\boldsymbol{a}_{\mathrm{SRP}} = \frac{\Phi_{\mathrm{S}}C_{\mathrm{R}}A}{m}\frac{AU^2}{u_{\odot}^3}\boldsymbol{u}_{\odot} \tag{24}$$

where Φ_{S} is the solar flux at Earth, C_{R} is the reflectivity coefficient, AU is the astronomical unit, and $\boldsymbol{u}_{\odot}$ is the vector from the sun to a given spacecraft.

Finally, the total acceleration for each spacecraft is calculated for the environment model.

$$\boldsymbol{a} = \boldsymbol{a}_{\mathrm{C}} + \boldsymbol{a}_{\mathrm{G}} + \boldsymbol{a}_{\mathrm{D}} + \boldsymbol{a}_{\mathrm{SRP}} \tag{25}$$

4. Control development

To investigate the robustness of the electrostatic actuation technique, a subset of the environmental perturbations described above are included in the controller: namely gravity, drag, and Coulomb accelerations. SRP is later included as an unmodeled perturbation. For control development, it is convenient to put the system in state-space form so that the state is defined $\boldsymbol{X} = [\boldsymbol{\rho}, \dot{\boldsymbol{\rho}}]^T$ and evolves according to the equation

$$\dot{\boldsymbol{X}} = \begin{bmatrix} \dot{\boldsymbol{\rho}} \\ \ddot{\boldsymbol{\rho}}(\boldsymbol{X}, \boldsymbol{V}) \end{bmatrix} \tag{26}$$

where $\dot{\boldsymbol{\rho}}$ is the relative velocity between the bodies observed in the inertial frame. Recall from previous discussion the notation $\dot{\boldsymbol{\rho}}$ denotes an inertial-frame time derivative of the vector [21].

The description in terms of relative state necessitates that relative accelerations be used in the derivation. These are calculated

$$\delta\boldsymbol{a}_i = \boldsymbol{a}_{\mathrm{F}_i} - \boldsymbol{a}_{\mathrm{L}_i} \tag{27}$$

where i is an index over the relevant perturbations. The relative Coulomb acceleration is derived given that Newton's 3rd law states that the these forces between the leader and follower are equal and opposite (i.e. $\boldsymbol{F}_{\mathrm{C_L}} = -\boldsymbol{F}_{\mathrm{C_F}}$).

$$\delta\boldsymbol{a}_{\mathrm{C}} = a_{\mathrm{C_F}} - a_{\mathrm{C_L}} = \frac{1}{m_{\mathrm{F}}}\boldsymbol{F}_{\mathrm{C_F}} - \frac{1}{m_{\mathrm{L}}}\boldsymbol{F}_{\mathrm{C_L}} = \frac{m_{\mathrm{F}} + m_{\mathrm{L}}}{m_{\mathrm{F}}m_{\mathrm{L}}}\boldsymbol{F}_{\mathrm{C_F}} = \frac{1}{m_{\mathrm{r}}}\boldsymbol{F}_{\mathrm{C_F}} \tag{28}$$

Here, the canonical reduced mass formula is recognized and denoted m_{r}.

4.1. Linearization of equations of motion

To apply linear control techniques, Eq. (26) must be linearized about some reference state and potential vector.

$$\dot{\boldsymbol{X}} \approx \dot{\boldsymbol{X}}(\boldsymbol{X}_0, \boldsymbol{V}_0) + \left.\frac{\partial\dot{\boldsymbol{X}}}{\partial\boldsymbol{X}}\right|_{\boldsymbol{X}_0}(\boldsymbol{X} - \boldsymbol{X}_0) + \left.\frac{\partial\dot{\boldsymbol{X}}}{\partial\boldsymbol{V}}\right|_{\boldsymbol{V}_0}(\boldsymbol{V} - \boldsymbol{V}_0) \tag{29}$$

The value $\dot{\boldsymbol{X}}(\boldsymbol{X}_0, \boldsymbol{V}_0)$ is the derivative of the state at the reference. Moving this term to the left side and using the Δ notation to indicate the difference between the variables and their reference values gives the familiar state-space form of the equations.

$$\Delta\dot{\boldsymbol{X}} = \left.\frac{\partial\dot{\boldsymbol{X}}}{\partial\boldsymbol{X}}\right|_{\boldsymbol{X}_0}\Delta\boldsymbol{X} + \left.\frac{\partial\dot{\boldsymbol{X}}}{\partial\boldsymbol{V}}\right|_{\boldsymbol{V}_0}\Delta\boldsymbol{V} \tag{30}$$

The general form of the expressions $\left.\frac{\partial\dot{\boldsymbol{X}}}{\partial\boldsymbol{X}}\right|_{\boldsymbol{X}_0}$ and $\left.\frac{\partial\dot{\boldsymbol{X}}}{\partial\boldsymbol{V}}\right|_{\boldsymbol{V}_0}$ are provided below in terms of the Jacobians of the state derivative with respect to the state and voltages, respectively.

$$\left.\frac{\partial\dot{\boldsymbol{X}}}{\partial\boldsymbol{X}}\right|_{\boldsymbol{X}_0} = [A] = \left.\begin{bmatrix} [0] & [I] \\ \frac{\partial\delta\boldsymbol{a}}{\partial\boldsymbol{\rho}} & \frac{\partial\delta\boldsymbol{a}}{\partial\dot{\boldsymbol{\rho}}} \end{bmatrix}\right|_{\boldsymbol{X}_0} \tag{31}$$

$$\left.\frac{\partial\dot{\boldsymbol{X}}}{\partial\boldsymbol{V}}\right|_{\boldsymbol{V}_0} = [B] = \left.\begin{bmatrix} [0] \\ \frac{\partial\delta\boldsymbol{a}}{\partial\boldsymbol{V}} \end{bmatrix}\right|_{\boldsymbol{V}_0} \tag{32}$$

The Jacobian of the Coulomb acceleration with respect to the state variable is complicated, as both the relative positions $\boldsymbol{r}_{1,i}$ and the capacitance matrix $[C]$ depend on the states as seen in Eqs. (5) and (7).

$$\begin{aligned} \frac{\partial\delta\boldsymbol{a}_{\mathrm{C}}}{\partial\boldsymbol{X}} = \frac{k_{\mathrm{C}}}{m_{\mathrm{r}}}\Bigg\{ &\left(\sum_{i=2}^{n}\frac{\boldsymbol{C}_i^T\boldsymbol{V}}{r_{1,i}^3}\boldsymbol{r}_{1,i}\right)\left(\boldsymbol{V}^T\frac{\partial\boldsymbol{C}_1}{\partial\boldsymbol{X}}\right) + \\ &\boldsymbol{C}_1^T\boldsymbol{V}\sum_{i=2}^{n}\left[\frac{\boldsymbol{r}_{1,i}}{r_{1,i}^3}\boldsymbol{V}^T\frac{\partial\boldsymbol{C}_i}{\partial\boldsymbol{X}} + \boldsymbol{r}_{1,i}\boldsymbol{C}_i^T\boldsymbol{V}\frac{\partial r_{1,i}^{-3}}{\partial\boldsymbol{X}} + \right. \\ &\left.\frac{\boldsymbol{C}_i^T\boldsymbol{V}}{r_{1,i}^3}\frac{\partial\boldsymbol{r}_{1,i}}{\partial\boldsymbol{X}}\right]\Bigg\} \end{aligned} \tag{33}$$

The derivative of the capacitance is necessarily a $n \times n \times 3$ tensor. Tensors of this shape are henceforth indicated with a double bar over the matrix, as shown in Eq. (34). Additionally, the prime notation here is used to denote the derivative with respect to the state. The derivative of the capacitance can be calculated by relation to the elastance, for which a simple analytic expression (Eq. (7)) exists.

$$\overline{\overline{[C']}} = \frac{\partial[C]}{\partial\boldsymbol{X}} = -[C]\overline{\overline{[S']}}[C] \tag{34}$$

Similar to the usage of capacitance vectors previously, the sub-matrices of the capacitance derivative are denoted $[C_i']$ henceforth.

$$\begin{aligned} \frac{\partial\delta\boldsymbol{a}_{\mathrm{C}}}{\partial\boldsymbol{X}} = \frac{k_{\mathrm{C}}}{m_{\mathrm{r}}}\Bigg\{ &\left(\sum_{i=2}^{n}\frac{\boldsymbol{C}_i^T\boldsymbol{V}}{r_{1,i}^3}\boldsymbol{r}_{1,i}\right)\boldsymbol{V}^T[C_1'] + \\ &\left(\boldsymbol{C}_1^T\boldsymbol{V}\right)\sum_{i=2}^{n}\frac{\boldsymbol{r}_{1,i}\boldsymbol{V}^T[C_i'] + \boldsymbol{C}_i^T\boldsymbol{V}([I] - 3\boldsymbol{r}_{1,i}\boldsymbol{r}_{1,i}^T)}{r_{1,i}^3}\Bigg\} \end{aligned} \tag{35}$$

The Jacobian of the Coulomb acceleration with respect to the control variable – the voltages on the follower and charge structure – is more straightforward, as the capacitance does not depend on this variable.

$$\frac{\partial\delta\boldsymbol{a}_{\mathrm{C}}}{\partial\boldsymbol{V}} = \frac{k_{\mathrm{C}}}{m_{\mathrm{r}}}\left\{\left(\sum_{i=2}^{n}\frac{\boldsymbol{C}_i^T\boldsymbol{V}}{r_{1,i}^3}\boldsymbol{r}_{1,i}\right)\boldsymbol{C}_1^T + (\boldsymbol{C}_1^T\boldsymbol{V})\sum_{i=2}^{n}\frac{\boldsymbol{r}_{1,i}\boldsymbol{C}_i^T}{r_{1,i}^3}\right\} \tag{36}$$

The matrices in Eqs. (35) and (36) are evaluated at the nominal follower position and potential vector, respectively, to obtain the linearized Coulomb dynamics and control in state space form as shown in Eq. (30). For the on-orbit scenario described previously, additional dynamics are present from relative orbital motion with drag. Under the assumptions of a circular leader orbit and nearby follower orbit, the formulation of the HCW equations with linearized drag forces presented first by Silva [22] and modified by Harris [23] is applied. These equations of motion typically include a secular differential drag acceleration which in this case is assumed to be canceled by the Coulomb repulsion between the leader and follower. Using these assumptions, the full system dynamics are produced by summing the state dynamics matrices of the HCW-plus-drag and Coulomb perturbed systems. The state dynamics and control sensitivity matrices are defined.

$$[A] = [A_{\mathrm{HCW+Drag}}] + \left.\begin{bmatrix} [0] & [I] \\ \frac{\partial\delta\boldsymbol{a}_{\mathrm{C}}}{\partial\boldsymbol{\rho}} & [0] \end{bmatrix}\right|_{\boldsymbol{X}_0} \tag{37}$$

$$[B] = \left.\begin{bmatrix} [0] \\ \frac{\partial\delta\boldsymbol{a}_{\mathrm{C}}}{\partial\boldsymbol{V}} \end{bmatrix}\right|_{\boldsymbol{V}_0} \tag{38}$$

Recall in the equations above that the controller does not include SRP accelerations.

Table 1
Minimal controllability summary.

Arrangement	Controllable eigenvectors
Single sphere	In-plane directions
Two spheres, In-plane	In-plane directions
Two spheres, Out-of-plane	All directions

4.2. Control law

A Linear Quadratic Regulator (LQR) controller is implemented on the system described. Control voltages $\boldsymbol{u}$ are sourced proportional to the deviation from the nominal state $\Delta\boldsymbol{X}$.

$$\boldsymbol{u} = [\mathcal{R}]^{-1}[B]^T[\mathcal{P}]\Delta\boldsymbol{X} = -[K]\Delta\boldsymbol{X} \tag{39}$$

Above, $[\mathcal{R}]$ is the control gain matrix and $[\mathcal{P}]$ is a solution to the algebraic Riccati equation which incorporates the state feedback gain $[Q]$ as well as $[A]$ and $[B]$. The gains $[\mathcal{R}]$ and $[Q]$ are tuned by trial and error to achieve a desired balance of state deviation and control usage.

5. Results & discussion

5.1. Linear controllability

Prior to examining linear controllability, the passive dynamics of the system are examined through eigenvalue analysis. The uncontrolled system is not stable – despite the potential well structure of the leader craft's electric field – as some of its poles exhibit positive real components. The control development described previously is specifically designed to yield stable linear closed-loop dynamics and indeed, all eigenvalues of $([A]-[B][K])$ have explicitly negative real components. It should be noted that this stability only holds as long as the linearization is valid, so large departures from the nominal state and control variables could result in instability.

Linear controllability can be readily established using the linearized equations of motion by analyzing the column and null space of the controllability matrix M.

$$M = \begin{bmatrix} B & AB & A^2B & \dots & A^nB \end{bmatrix} \tag{40}$$

Prior work on Coulomb-tethered spacecraft [24] and Coulomb-controlled formation flight [8] has suggested several results for this system's controllability. In a minimal sense, only the in-plane (HCW X-Y) states are found to be controllable with a single sphere on the leader spacecraft. While a single sphere could in theory produce only positive or negative accelerations in the HCW Y direction, controllability is achieved due to in-plane coupling in the HCW equations. Fundamentally, this result grounds the following results by replicating the controllability results found by Natarajan [10,25] with respect to a two-sphere formation actuated only by Coulomb attraction. Notably, due to the assumption of two-body motion, the out-of-plane mode is marginally stable and will remain bounded.

Out-of-plane controllability is achieved with the addition of a second sphere. Consider a charge structure similar to that in Fig. 1, but with only two spheres. Because the system has been linearized about an in-plane equilibrium, full controllability could not be achieved if the charge structure is arranged in-plane, i.e. along the HCW X axis. However, a line of charged spheres along the out-of-plane axis (HCW Z) yields full controllability in the position and velocity states, as the r_i states gain a component along the out-of-plane axis. These results are summarized in Table 1.

An additional limit on controllability is established by Eq. (21). If this condition is not met, the along-track drag acceleration cannot be balanced and the control cannot stabilize the system.

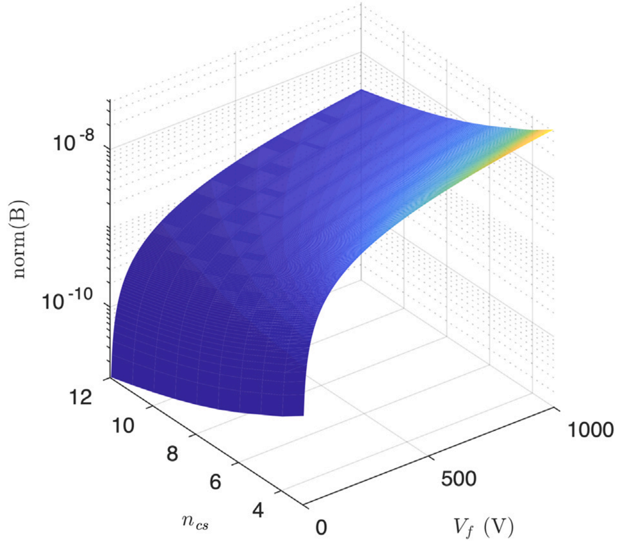

Fig. 3. norm($[B]$) variation with respect to n and V_f.

5.2. Control sensitivity

With the linear controllability of the system established, it is necessary to further examine the sensitivity of prospective controllers to the selection of multiple system parameters. A major concern with this approach is the validity of the linearization under large control voltages. As such, the selection of system parameters should minimize the control voltage requested by the controller. In an equivalent sense, it is desirable for changes from the reference voltage to have a large impact on the system's states. For a linear system, the impact of these parameters is governed by the control effect matrix B. For systems that satisfy the necessary conditions for controllability derived in Section 5.1, the Frobenius norm of B is used as an index of control sensitivity with respect to parameter variation.

$$\text{norm}([B]) = \sqrt{\sum_{i=1}^{m}\sum_{j=1}^{n}|B_{ij}|^2} \tag{41}$$

The sensitivity of B with respect to the follower voltage V_f and the number of spheres constituting the charge structure n_{cs} was evaluated for a range of plausible values of n_{cs} and V_f, resulting in Fig. 3. The norm of B scales log–logarithmically as V_f increases, as each sphere carries a larger voltage under nominal conditions. At the same time, the norm of B drops as the number of spheres increases, reflecting the fact that attractive and repulsive forces between spheres cancels out some degree of controllability. These results show that the norm of B is largest when the charge structure consists of only a handful of spheres and the follower maintains a relatively large voltage.

Using $n_{cs} = 2$ and $V_f = 1000$ V, the sensitivity of norm($[B]$) was investigated with respect to the charge structure radius (R_{cs}), and the radii scale R_s/R_{cs}, which is constrained to be less that 1 such that no spheres have overlapping volumes as mentioned previously. These results are shown in Fig. 4. Here, it is apparent that the norm of $[B]$ increases with both the charge structure radius and the radii of the spheres constituting the charge structure. As the charge structure radius increases, additional control authority is achieved by the larger components of the forces resulting from each sphere along axes other than the HCW Y direction. Similarly, as the sphere radii increase, the electric field generated by each sphere for a given voltage increases in magnitude, resulting in larger forces on the follower.

From these sweeps, it is apparent that a system designed for maximized control effectiveness will use the largest feasible charge structure radius (R_{cs}), sphere radii (R_s), and follower voltage while minimizing

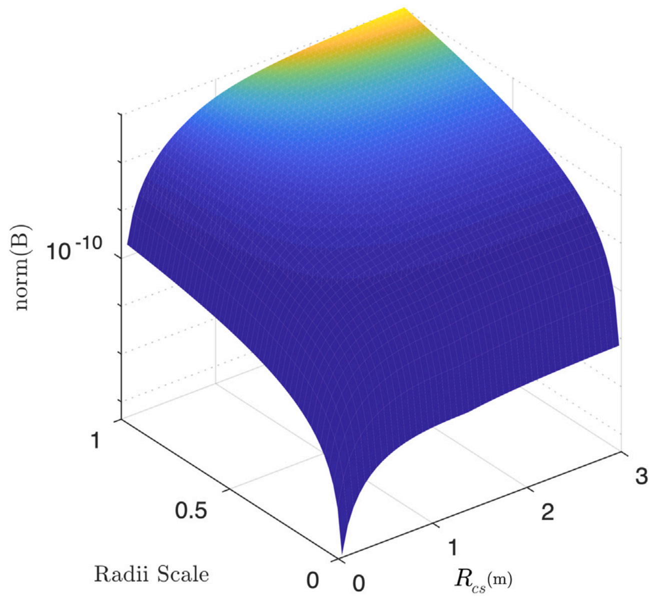

Fig. 4. norm([B]) variation with respect to the charge structure radius R_{cs} and dimensionless radii scale $R_{\mathrm{s}}/R_{\mathrm{cs}}$.

Table 2
Maximum control norm design parameters.

Parameter	Value
V_{f}	−1000 V
n_{cs}	2
R_{cs}	3 m
R_{s}	2.5 m

the number of spheres used. As discussed previously, instances of in-wake charging of up to −6 kV have been observed in LEO. [16] However, large voltages may require extremely large power if the wake collapses. The case of the Space Shuttle charging used many Watts of power (the wake likely collapsed) which is not feasible for the electrostatic actuation system. On the other hand, the pusher-only control technique motivated by the asymmetric shielding in the wake [19] demands that only negative voltages are sourced. The nominal follower voltage of −1000 V fit both criterion for the simulations to follow.

Another concern discussed previously is that arcing and other charging effects occur if $R_{\mathrm{s}} \approx R_{\mathrm{cs}}$, so R_{s} is chosen such that the two charged spheres will be separated by 1 meter — a sufficient distance to mitigate the likelihood of arcing at LEO densities, though calculation of this distance requires detailed knowledge of the plasma in the wake.

5.3. Simulation results

Simulations are performed applying the linear control law derived above to the nonlinear dynamics in two different cases. The controller is run at 0.2 Hz and control gains are chosen such that the system settles within ~45 min (0.5 orbits). The orbit elements – given in order, semi-major axis, eccentricity, inclination, right ascension, argument of periapsis, and true anomaly – of the leader are $[7000\ \mathrm{km}, 0, 0°, 0°, 20°, 0°]^T$. The relative drag and SRP perturbations are similar in magnitude at this altitude. Therefore, this orbit provides a good test of robustness for the controller, which does not include SRP dynamics. A nominal separation distance of 1 m in the along-track direction is chosen to fit the requirements of a DCPA mission.

For direct comparison with the discussion immediately above, an initial simulation is performed applying the parameters outlined in Table 2. Additionally, perfect knowledge of the constant relative drag acceleration and of the follower craft's HCW position is assumed as is the ability to perfectly source voltage on each sphere. These parameters and assumptions will be changed in later simulations. The performance of the control is considered for a case in which the follower is offset from the nominal position – about which the linearization is performed – by 1 cm in the along-track direction.

Table 3
Mission scenario design parameters.

Parameter	Value
V_{f}	−1000 V
n_{cs}	3
R_{cs}	0.3 m
R_{s}	0.25 m

Table 4
System physical parameters.

Parameter	Leader	Follower
Area (m^2)	0.5	0.008
Mass (kg)	1000	1
Coefficient of reflectivity	1	1
Coefficient of drag	2.2	0

Note that the signature of the plot in Fig. 6 resembles the step response of a forced, damped harmonic oscillator. The linearized equations of motions within the controller shown in Eqs. (32), (37), and (38) bear out this behavior as a step function in follower position is applied. The initial increase in separation distance before the control settles to the nominal value results because only two spheres are used in the charge structure. Table 1 indicates that two spheres placed symmetrically out of plane results in a fully controllable system, but this is due to the coupling in the HCW X and Y directions. This is illustrated in Fig. 7, which shows the offset from nominal for each of the HCW directions.

If the controller simply pulled the sphere in the along-track direction, some radial change would occur. Two spheres out of plane cannot generate an electric field to fully control in this direction — only with the HCW dynamics is the system fully controllable. By leveraging the system dynamics, and specifically the known in-plane coupling exhibited by the HCW equations, the system is able to stabilize with the help of the controller. The control voltages in Fig. 5 shows the deviation from the nominal voltages for the follower and for spheres 1 and 2 on the charge structure denoted as S_1 and S_2, respectively. Note that the line for S_1 cannot be seen because identical voltages are commanded on the two leader-craft spheres. The maximum deviation from the nominal voltage for this case (~60 V) is small, resulting in a linearization error of roughly 5% in the Coulomb force acceleration magnitude.

While the simulation above demonstrates the effectiveness of the control given parameters that enhance controllability, the values in Table 2 and the assumptions state above do not fit a realistic mission scenario. The parameters in Table 3 are used in the simulation to follow which as before attempts to regulate the follower at a 1 m separation in the anti-alongtrack direction. They are chosen to be commensurate with the dimensions of the leader shown in Table 4. After running simulations, the number of spheres in the charge structure on the leader was increased to improve the system settling behavior as noise and unmodeled perturbations are included in this latter case. Note from Table 3 that the conducting sphere surfaces are extremely close ~1 mm. This indicates that arcing could occur for significant voltage differences between the spheres. This effect is ignored for this baseline analysis.

The size and mass of the leader craft were based roughly on the Iridium spacecraft to provide a reasonable baseline for a LEO mission. The follower is assumed to be a spherical craft small enough to fit within the wake of the leader. To simulate the effects of the wake on atmospheric drag, the drag coefficient of the follower is nulled.

The previous assumption that the follower position is known perfectly is relaxed. White Gaussian noise of $\sigma_r = 10^{-3}$ m, $\sigma_v = 10^{-5}$m/s is

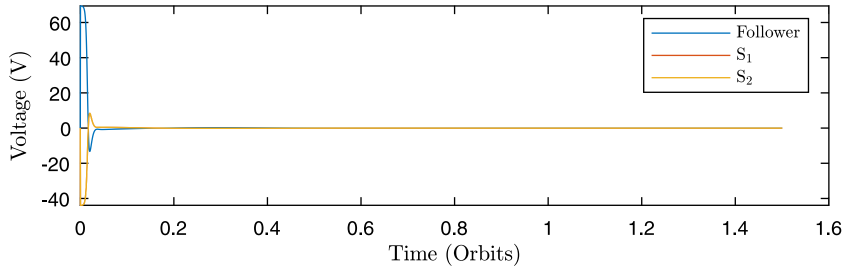

Fig. 5. Deviation of system voltages from nominal. The curve for S_2 is superimposed on the identical curve for S_1.

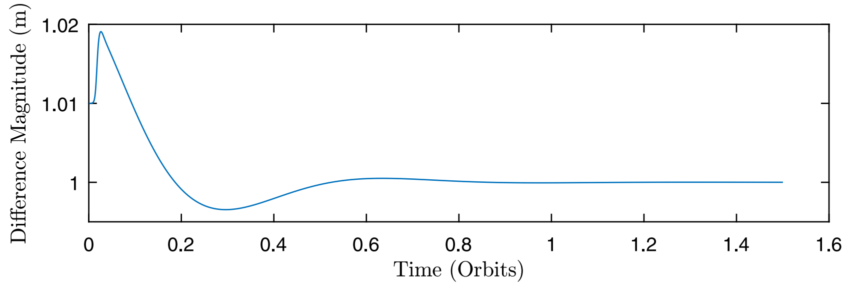

Fig. 6. HCW-frame follower position magnitude for perfect feedback system.

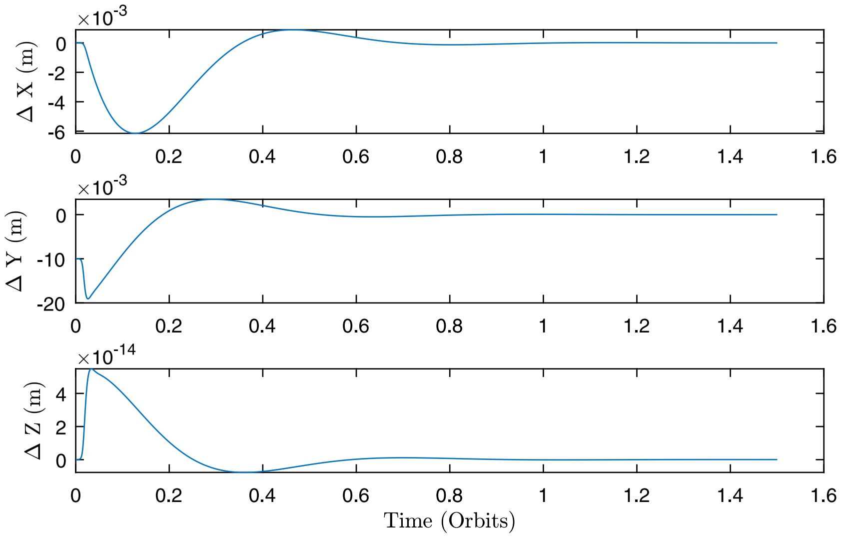

Fig. 7. HCW vector component differences.

added to the range value input to the controller. To account for this, a simple averaging filter is applied, running at a lower frequency than the measurements are coming in. Ten range measurements are averaged while the control voltages are held constant.

Solar Radiation Pressure (SRP) is included as an unmodeled perturbation. Both drag and SRP vary as they pass in and out of sunlight. Drag is varied sinusoidally by ±30% to roughly reflect density changes between sun and eclipse [26], while SRP is cut completely in shade. These simplified models are described in greater detail in Table 5 where ν is the true anomaly. A clear distinction is made between the controller dynamics and simulated environment.

Finally, the simulation is initialized with a 1 cm offset in the HCW Y direction as before. Fig. 8 shows the control performance of the system. With unmodeled accelerations and noisy range measurements, the system remains within $\sim$1 mm of the nominal position after the initial 1 cm offset is corrected. The ability of the control to remain exactly at this location is compromised, however it does stay extremely close — well within the sub-centimeter accuracy required by DPCA.

Table 5
SRP and drag models in simulation.

	Drag	SRP
Controller	$\rho_{atm} = \rho_{atm,0}$	$C_R = 0$
Environment	$\rho_{atm} = \rho_{atm,0}(1 + 0.3\sin(\nu))$	$C_R = \begin{cases} C_R & 0 \le \nu < \pi \\ 0 & \pi \le \nu < 2\pi \end{cases}$

Fig. 9 shows the deviation of system voltage from the nominal sourced at a given time step. The pusher-only control described in previous sections is sufficient, as no positive voltages are sourced. Note that the voltages sourced by the controller in this latter simulation are much large than those in the previous simulation. While larger negative voltages are more likely to collapse the wake as mentioned previously, the voltage at which this occurs is extremely difficult to determine giving the complexity of plasma dynamics.

This results from the addition of noise on the follower position and the change in the system parameters. As indicated previously, a

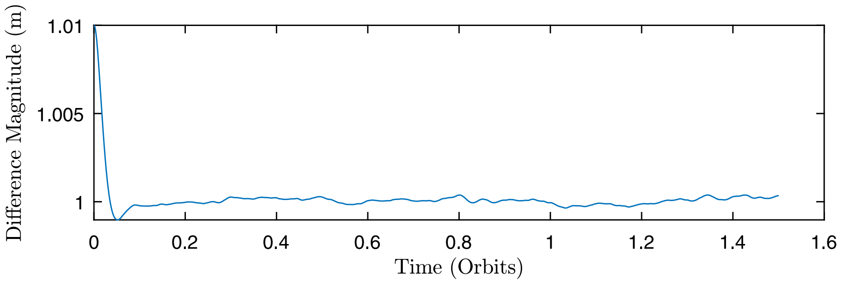

Fig. 8. HCW-frame follower position magnitude.

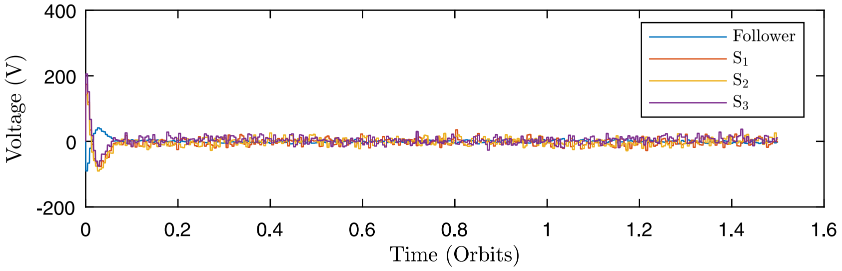

Fig. 9. Deviation of system voltages from nominal.

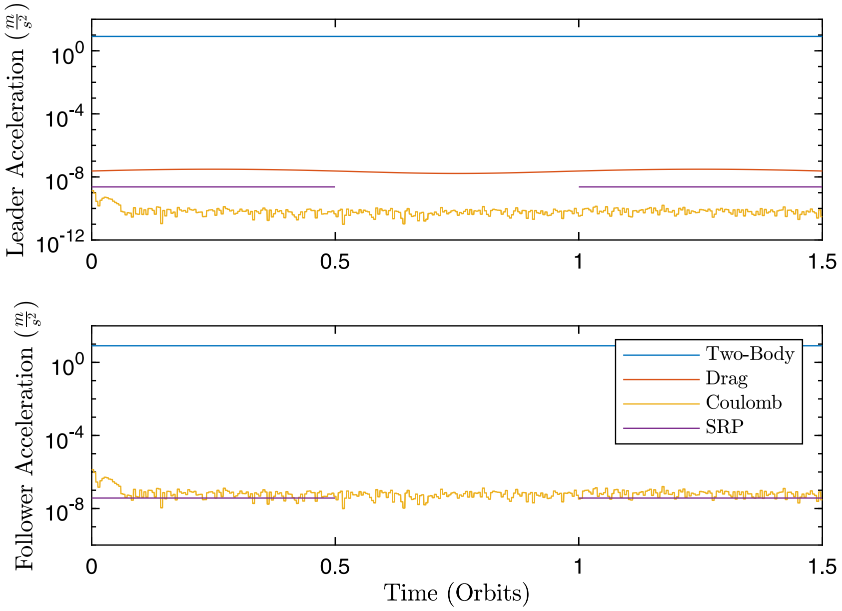

Fig. 10. Drag, Coulomb, and SRP accelerations on the leader and follower crafts.

very large voltage must be sourced to generate a very small relative acceleration. Therefore, even the relatively small position and velocity errors incurred from incorporating noise in the system generate a very large control response. The previous case's controller was not met with any unmodeled perturbations and therefore experiences more consistent, smaller state errors.

The drag, Coulomb, and SRP accelerations are shown for both the leader and follower in Fig. 10. Recall that the drag acceleration of the follower is nulled according to the assumptions discussed previously. Note that the drag acceleration dominates the Coulomb acceleration for the leader craft. This is because the equal and opposite Coulomb force produces a much smaller acceleration due to the large mass of the leader.

The relative accelerations between the leader and follower are displayed in Fig. 11. Note here that, once the system has settled, the relative Coulomb acceleration remains similar to the total perturbation magnitude – the sum of the gravitational, drag, and SRP relative accelerations – when in the sun, but does not decrease with the total perturbation magnitude as the spacecraft pass into shade. This is because the controller is still correcting on the noise added to the system.

Fig. 12 shows the linearization error in the Coulomb acceleration over the simulation duration. The linearized acceleration was calculated using Eqs. (35) and (36) and the state and voltage offsets at a given timestep, while the nonlinear acceleration is calculated directly with Eq. (12). These errors are bounded within about ±20%, though at most times it is much smaller than this. However, for larger initial condition offsets, these errors grew large enough that the controller could not stabilize the system. This results from the fact that, unlike with most actuators, the control authority of the electrostatic actuation

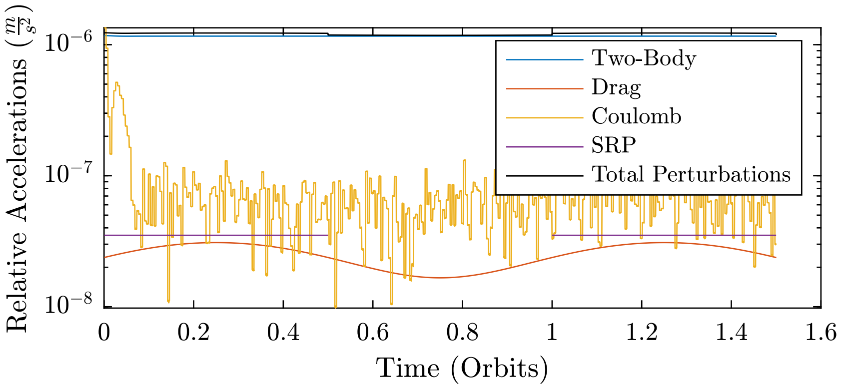

Fig. 11. Relative accelerations between the leader and follower crafts. The sum of the gravity, drag, and SRP relative accelerations is shown in black for reference.

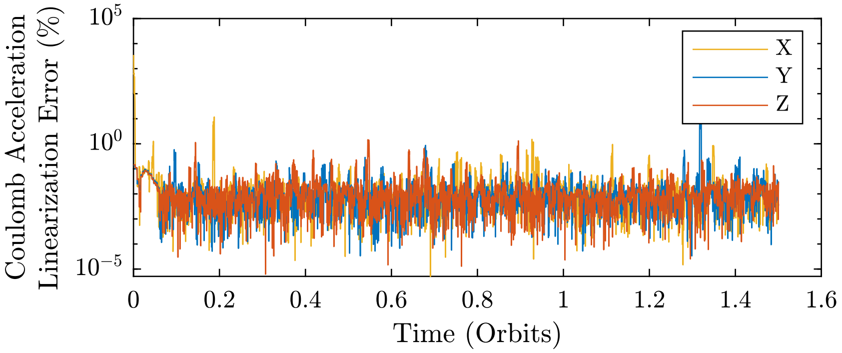

Fig. 12. Coulomb acceleration linearization error.

technique drops off as the inverse square of the relative distance. This in effect means control authority is being lost at larger distances. The controller cannot account for this nonlinear behavior, resulting in instability despite the linear system being stable. To provide context, an initial offset of 6 cm results in system instability given the parameters in the second simulation. This is a significant weakness of the chosen control methodology. Future work will attempt to mitigate these linearization errors.

6. Conclusion & future work

Coulomb actuation is applied to close-proximity leader–follower formation with the goal of maintaining relative position with high precision. The DPCA mission concept is used to guide the generation of feasible parameters. A formulation of the Coulomb acceleration is provided using MSM, and is then linearized about the state and control variables for application to a linear controller. The nonlinear dynamics are also used to generate a minimum follower voltage for a given system geometry (Eq. (21)), which provides additional feasibility insight. Linear controllability is assessed on a system with the linearized Coulomb acceleration as well as linearized HCW and drag, and parameters are chosen to reduce the control norm. Simulations are performed with these and the system is shown to stabilize the follower position about the nominal even under unmodeled perturbations and sensor noise. Finally, more mission-appropriate parameters and assumptions are used in a simulation which demonstrates that the controller still functions, though not as well as in the idealized case.

Declaration of competing interest

The authors declare that they have no known competing financial interests or personal relationships that could have appeared to influence the work reported in this paper.

References

[1] Gordon Roesler, Robotic servicing of geosynchronous satellites (RSGS) proposers day briefing prepared for robotic servicing of geosynchronous satellites (RSGS) proposers day, 2016.
[2] Niels H. Roth, Ben Risi, C. Cordell Grant, Robert E. Zee, Flight results from the CanX-4 and CanX-5 formation flying mission, 4S Symp. (1) (2016) 1–15.
[3] David A. Vallado, Fundamentals of Astrodynamcs and Applications, fourth ed., Space Technology Library, 2013.
[4] Cyrus Foster, Henry Hallam, James Mason, Orbit determination and differential-drag control of planet labs cubesat constellations, Adv. Astronaut. Sci. 156 (2016) 645–657.
[5] Frank Marcos, Bruce Bowman, Robert Sheehan, Accuracy of earth's thermospheric neutral density models, in: AIAA/AAS Astrodynamics Specialist Conference and Exhibit, 2006, pp. 1–20.
[6] Marcin D. Pilinski, Brian M. Argrow, Scott E. Palo, Drag coefficients of satellites with concave geometries: Comparing models and observations, J. Spacecr. Rockets 48 (2) (2011) 312–325.
[7] Christopher J. Capon, Melrose Brown, Russell R. Boyce, Charged aerodynamics of a low earth orbit cylinder, in: AIP Conference Proceedings, Vol. 1786, 2016.
[8] Lyon B. King, Gordon G. Parker, Satwik Deshmukh, Jer-Hong Chong, Spacecraft formation-flying using inter-vehicle coulomb forces, NIAC Phase I Final Report, 2002.
[9] Hanspeter Schaub, Gordon G Parker, Lyon B King, Jan June, Challenges and prospects of coulomb spacecraft formation control of the astronautical sciences challenges and prospects of coulomb spacecraft formation control, J. Astronaut. Sci. 52 (2004) 169–193.
[10] Arun Natarajan, Hanspeter Schaub, Linear dynamics and stability analysis of a two-craft coulomb tether formation, Adv. Astronaut. Sci. 120 (II) (2005) 1635–1649.
[11] Daan Stevenson, Hanspeter Schaub, Multi-sphere method for modeling spacecraft electrostatic forces and torques, Adv. Space Res. 51 (1) (2013) 10–20.
[12] Jordan Maxwell, Kieran Wilson, Joseph Hughes, Hanspeter Schaub, Multisphere method for flexible conducting space objects: Modeling and experiments, J. Spacecr. Rockets (2019) 1–10.
[13] D.E. Hastings, A review of plasma interactions with spacecraft in low earth orbit, J. Geophys. Res. 100 (A8) (1995) 14457–14483.
[14] Jordan Maxwell, Hanspeter Schaub, Low earth orbit plasma wake shaping and applications to on-orbit proximity operations, in: Spacecraft Charging Technology Conference, Kobe, Japan, June 25-29 2018, P-A-4.

[15] C.J. Capon, M. Brown, R.R. Boyce, Scaling of plasma-body interactions in low earth orbit, Phys. Plasmas 24 (4) (2017) 042901.
[16] William Hall, Philip Leung, Ira Katz, Garya Jongeward, John Lilley, Polar-auroral charging of the space shuttle and EVA astronaut, in: AGARD, The Aerospace Environment at High Altitudes and its Implications for Spacecraft Charging and Communications 9 p(SEE N 87-26937 21-18), 1987.
[17] S.L. Durden, P.R. Siqueira, S. Tanelli, On the use of multiantenna radars for spaceborne doppler precipitation measurements, IEEE Geosci. Remote Sens. Lett. 4 (1) (2007) 181–183.
[18] S. Tanelli, S.L. Durden, M.P. Johnson, Airborne demonstration of DPCA for velocity measurements of distributed targets, IEEE Geosci. Remote Sens. Lett. 13 (10) (2016) 1415–1419.
[19] Benoit Durand de Gevigney, Thomas Sunn Pedersen, Allen H Boozer, Debye screening and injection of positrons across the magnetic surfaces of a pure electron plasma in a stellarator, Phys. Plasmas 18 (1) (2011) 013508.
[20] William B. Smythe, Static and dynamic electricity, 1988.
[21] Hanspeter Schaub, John L. Junkins, Analytical Mechanics of Space Systems, in: fourth ed., AIAA Education Series, Reston, VA, 2018.
[22] Elvis D. Silva, A formulation of the clohessy-wiltshire equations to include dynamic atmospheric drag, in: AIAA/AAS Astrodynamics Specialist Conference, 2008, (August).
[23] Andrew T. Harris, Christopher Petersen, Hanspeter Schaub, Linear coupled attitude-orbit control through aerodynamic forces, in: 2018 Space Flight Mechanics Meeting, 2018, pp. 1–13, (January).
[24] Arun Natarajan, Hanspeter Schaub, Linear dynamics and stability analysis of a coulomb tether formation, J. Guid. Control Dyn. 29 (4) (2006) 831–839.
[25] Arun Natarajan, Hanspeter Schaub, Gordon G Parker, Arun Natarajan, Hanspeter Schaub, Gordon G Parker, Reconfiguration of a nadir-pointing 2-craft coulomb tether, J. Br. Interplanet. Soc. 60 (6) (2007) 209–218.
[26] Sean L. Bruinsma, Jeffrey M. Forbes, Medium-to large-scale density variability as observed by CHAMP, Space Weather 6 (8) (2008).